Superstructural ordering in coacervate-based protocell networks

- Wenjing Mu^{1,2}, Liyan Jia^{1,2}, Yiyang Lin^{3*}, Musen Zhou⁴, Jianzhong Wu⁴, Stephen Mann^{5,6,7*} and Yan Qiao^{1,2*}
- 5 ¹ Beijing National Laboratory for Molecular Sciences (BNLMS), Laboratory of Polymer Physics and Chemistry,
- 6 CAS Research/Education Center for Excellence in Molecular Sciences, Institute of Chemistry, Chinese Academy of Sciences, Beijing 100190, China.
- 8 ² University of Chinese Academy of Sciences, Beijing 100049, China.
- 9 ³ State Key Laboratory of Chemical Resource Engineering, Beijing Laboratory of Biomedical Materials, Beijing 10 University of Chemical Technology, Beijing 100029, China.
- 11 ⁴ Department of Chemical and Environmental Engineering, University of California, Riverside, CA 92521, USA.
- 5 Centre for Protolife Research and Centre for Organized Matter Chemistry, School of Chemistry, University of
 Bristol, Bristol BS8 1TS, United Kingdom.
- Max Planck-Bristol Centre for Minimal Biology, School of Chemistry, University of Bristol, Bristol BS8 1TS, United Kingdom.
- ⁷ School of Materials Science and Engineering, Shanghai Jiao Tong University, Shanghai 200240, P. R. China.
- 18 *Corresponding author email: y.lin@mail.buct.edu.cn (Y.L.); S.Mann@bristol.ac.uk (S.M.); 19 yanqiao@iccas.ac.cn (Y.Q.)

The bottom-up assembly of higher-order cytomimetic systems capable of coordinated physical behaviours, collective chemical signalling and spatially integrated processing is a key challenge in the study of artificial multicellularity. Here we develop an interactive binary population of coacervate micro-droplets that spontaneously self-organize into chain-like protocell networks with an alternating sequence of structurally dissimilar micro-domains and hemi-spherical contact points. The protocell superstructures exhibit macromolecular self-sorting, spatially localized enzyme/ribozyme biocatalysis and inter-droplet molecular translocation, are capable of topographical reconfiguration using chemical or light-mediated stimuli and can be used as a micro-extraction system for macroscale biomolecular sorting. Our methodology opens a pathway to the self-assembly of multi-component protocell networks based on selective processes of coacervate droplet-droplet adhesion and fusion and provides a step towards the spontaneous orchestration of protocell models into artificial tissues and colonies with ordered architectures and collective functions.

Introduction

Organization of artificial cell-like compartments (protocells) into interconnected protocell networks offer opportunities to study aspects of artificial multicellularity such as long-range programmable signalling¹, controlled protein expression², morphogen-mediated differentiation³ and utilization of externally stored energy⁴. Building higher-order cytomimetic systems is timely because numerous protocell models are currently available, including lipid vesicles⁵⁻⁷, polymersomes⁸⁻⁹, proteinosomes¹⁰, colloidosomes¹¹⁻¹³,

polysaccharidosomes^{14,15}, and membrane-less^{16,17} or membranized¹⁸⁻²¹ coacervate micro-droplets. Taken together, these synthetic constructs exhibit a diversity of life-like properties such as cell-free gene expression²², DNA transcription^{23,24}, growth, division and fusion²⁵⁻²⁷, biochemical activity²⁸⁻³¹, sensing and motility^{32,33}, phagocytosis³⁴ and predation^{35,36} that are associated with the endogenous activity of discrete protocells or their contact-dependent interactivity. Extending these attributes into higher-order networks necessitates the controlled assembly and ordering of protocell populations in space and time³⁷, and has been achieved principally through the use of external manipulation involving 3D printing³⁸⁻⁴⁰, acoustic force fields⁴¹, magnetic fields⁴² micro-pipetting⁴³ and microfluidics^{44,45}. In contrast, although randomly organized tissue-like colonies of protocells have been prepared using interfacial click chemistry^{46,47} or hydrogel immobilization⁴⁸, the spontaneous bottom-up assembly of organized protocell networks without external manipulation or energy input remains a considerable challenge.

43 44

45

46 47

48

49

50

51

5253

54

55

56

57

58

59

60

61

62

63

64

65

66

67

68

69

70

71 72

73

74

75

76

77

78

In this work, we report the spontaneous self-organization of reconfigurable chain-like protocell networks capable of macromolecular self-sorting, spatially localized biocatalysis, and inter-droplet molecular translocation (Fig. 1). We show that associative liquid-liquid phase separation in a ternary mixture of a double-tailed quaternary cationic amphiphile ammonium (didodecyldimethyl bromide, DDAB), а cationic polyelectrolyte (poly(diallyldimethylammonium chloride, PDDA) and a photoactive anionic aspartic acid-appended azobenzene derivative (trans-AzoAsp2, Supplementary Fig. S1) produces a binary population of immiscible DDAB/trans-AzoAsp2 and PDDA/trans-AzoAsp2 coacervate micro-droplets with liquid crystalline and homogeneous internal structures, respectively. The coacervate droplets spontaneously self-organize into linear and branched chains with an alternating sequence of structurally dissimilar micro-domains and hemi-spherical contact junctions. By recruiting different biomacromolecules into specific domains of the protocell chains we implement spatially localized enzyme- or ribozyme-mediated reactions within the self-assembled networks. The chain-like arrays can be topologically reconfigured by selective domain disassembly arising from host-guest complexation of β-cyclodextrin (β-CD)⁴⁹ within the DDAB/trans-AzoAsp₂ coacervate droplets. Alternatively, fusion of the immiscible coacervate droplets within the networks and reversible transfer of guest molecules can be induced by photo-isomerisation of AzoAsp₂50. Finally, we develop a protocell network-based micro-extraction and macroscale biomolecular sorting system by exploiting differences in coacervate density to release and separate the interconnected droplets and their constituent macromolecular cargoes. Taken together, our results demonstrate that superstructural ordering of dissimilar coacervate droplets can be achieved spontaneously by selective droplet-droplet adhesion and fusion, open a pathway to the self-assembly of multi-component protocell networks and provide a step towards higher-order cytomimetic systems capable of selective sorting and spatially integrated chemical processing.

81 82

83

84

85

86

8788

89

90

91

92

93

94

95

96

97

98

99

100

101

102

103

104105

106

107

108

109

110

111

112

113

79

80

Results and discussion

Protocell network components and assembly

We prepared populations of immiscible DDAB/trans-AzoAsp2 and PDDA/trans-AzoAsp2 coacervate droplets as the basis for constructing a higher-order multi-component protocell network. First, we investigated the individual coacervate systems prior to self-assembly. In both cases, mixing aqueous solutions of DDAB and trans-AzoAsp₂ or PDDA and trans-AzoAsp₂ at a DDAB/trans-AzoAsp₂ or PDDA/trans-AzoAsp₂ molar ratio of 4:1 gave rise to positively charged coacervate micro-droplets (typical zeta potentials; +37 mV (DDAB/AzoAsp₂) and +8 mV (PDDA/AzoAsp₂), usually less than 10 μm in diameter. The DDAB/trans-AzoAsp2 coacervate droplets were readily imaged by fluorescence microscopy using the hydrophobic fluorophore, Nile Red, which was sequestered into the coacervate phase (Fig. 2a). Polarized optical microscopy (POM) images on single droplets showed intense birefringent Maltese-cross patterns (Fig. 2b), which disappeared after incubation at 90 °C for 15 min, indicative of a liquid crystalline DDAB/trans-AzoAsp₂ coacervate⁵¹. Conversely, the PDDA/trans-AzoAsp2 droplets preferentially accumulated hydrophilic fluorophores such as 8-hydroxypyrene-1,3,6-trisulfonic acid (HPTS) and showed no birefringence (Figs. 2c,d), indicating a homogeneous coacervate matrix with a relatively high dielectric constant. Fluorescence recovery after photobleaching (FRAP) measurements⁵² showed slow (80% within 900 s) or fast (90% within 30 s) fluorescence recovery in Nile Red-loaded DDAB/trans-AzoAsp2 or HPTS-loaded PDDA/trans-AzoAsp2 coacervate droplets, respectively (Figs. 2e,f) with corresponding estimated apparent diffusion coefficients of 9.3 \times 10⁻¹⁵ and 5.6 \times 10⁻¹⁴ m²/s⁵³. The approximately 6-fold increase in fluorophore mobility within the PDDA/trans-AzoAsp2 micro-droplets was attributed to the restricted lateral diffusion of Nile Red in the liquid crystalline matrix of the DDAB/trans-AzoAsp2 phase. Moreover, the increased hydrophobicity of the liquid crystalline DDAB/trans-AzoAsp2 phase increased the stability of the droplets against salt-induced dissolution (Figs. 2g,h).

Spontaneous assembly of ordered protocell networks was achieved by mixing DDAB, PDDA and *trans*-AzoAsp₂ at a corresponding molar ratio of 4 : 4 : 2 at room temperature for 50 min. Fluorescence microscopy images showed predominantly self-organized microstructures in the form of linear and branched chain-like networks consisting of an alternating sequence of interconnected DDAB/*trans*-AzoAsp₂ and PDDA/*trans*-AzoAsp₂

coacervate micro-droplets (**Fig. 3a, Supplementary Fig. S2**). The immiscible droplets were typically less than 10 µm in size and adhered to each other with distinct hemispherical contact points. Fluorescence intensity profiles along the chains (**Supplementary Fig. S3**), as well as POM images (**Supplementary Fig. S4**) and FRAP measurements (**Supplementary Fig. S5**) confirmed the alternating positioning of the different droplets. Formation of the higher-order assemblies was observed irrespective of the order in which DDAB, PDDA and *trans*-AzoAsp₂ were added (**Supplementary Fig. S6**), indicating that droplet self-organization occurred under thermodynamic conditions.

Time-dependent plots of forward light scattered area (FSC-A) versus side light scattered area (SSC-A) derived from fluorescence-activated cell sorting (FACS) measurements over 90 min showed the progressive emergence of a peak in the maximum FSC-A count (Figs. 3b-e), which was attributed to increasing numbers of chain-like assemblies. The mechanism of chain ordering was monitored using time-lapse fluorescence microscopy. Upon mixing of DDAB, PDDA and trans-AzoAsp₂, attractive interactions between the DDAB/trans-AzoAsp₂ and PDDA/trans-AzoAsp₂ coacervate droplets gave rise to pairwise combinations and small partially organized clusters that increased in length and droplet size typically over a period of 60 min (Supplementary Fig. S7 and Movie S1). Ordering within the networks increased with time due to intra-cluster fusion events, which specifically merged droplets of the same type that were sufficiently close to each other, leaving only a regularly interspersed arrangement of self/non-self cohesive connections (Figs. 3f-i).

Alternate positioning of the DDAB/trans-AzoAsp2 and PDDA/trans-AzoAsp2 coacervate droplets was most prominent in networks produced when the number density of both types of droplets was approximately equal (DDAB: PDDA = 1:1) (Fig. 3j). Under these conditions, the rates of self/non-self droplet adhesion and self/self droplet coalescence in the initially formed clusters were effectively matched so that regular interspersing of discrete droplets gave rise to a relatively stable micro-structure. In contrast, increasing the amount of PDDA (DDAB: PDDA = 1:2; 1:3) resulted in larger diffuse PDDA/trans-AzoAsp2 domains that were often distributed between well-defined DDAB/trans-AzoAsp2 droplets (Fig. 3j). Lower PDDA concentrations did not appear to significantly disrupt the network architecture, presumably because the DDAB/trans-AzoAsp2 droplets were less susceptible to coalescence (Supplementary Fig. S8).

The relative interfacial tensions (γ_{DDAB} , γ_{PDDA} and $\gamma_{DDAB/PDDA}$) at the coacervate droplet junctions and the corresponding three-phase contact angles (θ_{DDAB} and θ_{PDDA} ; θ = 180 ° (complete dewetting)) between the micro-droplets were determined by image analysis of the fluorescence microscopy images (**Fig. 3k**)^{54,55}. Values of θ_{DDAB} determined for different DDAB : PDDA molar ratios remained within a relatively narrow range (135-150°), while θ_{PDDA}

was smaller and dependent on the DDAB : PDDA molar ratio (**Fig. 3I**). Specifically, a maximum θ_{PDDA} value of 125° was measured at a DDAB : PDDA molar ratio of 1 : 1, corresponding to stable alternating sequences of interconnected coacervate droplets. Lower θ_{PDDA} angles ranging from 115° to 55° were observed at higher or lower DDAB : PDDA molar ratios (**Fig. 3I**), consistent with increased levels of wetting at the droplet junctions. Notably, the DDAB/*trans*-AzoAsp₂ droplets were relatively unperturbed on contact with the PDDA/*trans*-AzoAsp₂ domains ($\theta_{DDAB} > \theta_{PDDA}$), implying that $\gamma_{DDAB/PDDA}$ was higher than γ_{DDAB} , and $\gamma_{DDAB/PDDA}$ greater than γ_{PDDA} , consistent with the liquid crystalline structure of the DDAB/*trans*-AzoAsp₂ droplets.

158159160

161

162

163

164

165

166

167

168

169

170

171

172

173

174

175

176

177

178

179

180

181

182

183

184

150

151

152

153

154

155

156

157

Biomolecular organization and processing in protocell networks

Given that alternating sequences of immiscible and structurally dissimilar coacervate droplets could be interconnected within chain-like arrays, we sought to utilise the networks as a platform for constructing a functional multi-component protocell model with higher-level organization. Based on their distinct composition and structuration, we reasoned that the immiscible coacervate droplets would be able to preferentially sequestrate different biomolecules from the external environment, thereby providing a mechanism for spatially selective molecular partitioning, leading to protocell networks with regiospecific properties and localized chemical processing (Fig. 4a). We tested the selectivity of biomolecular uptake by exposing the coacervate droplet assemblies to mixtures of fluorescently labelled proteins, oligonucleotides and lipids and monitoring the spatial distribution of the guest molecules by fluorescence microscopy. Images recorded using mixtures of rhodamine isothiocyanate-modified horseradish peroxidase (RITC-HRP) and carboxyfluorescein-modified ssDNA (FAM-ssDNA) showed high levels of spatial sorting within the networks with RITC-HRP or FAM-ssDNA distributed preferentially in the DDAB/trans-AzoAsp₂ or PDDA/trans-AzoAsp₂ coacervate droplets, respectively (Figs. 4b,c). Similarly, binary mixtures of oligonucleotides and polysaccharides (ssDNA/DEAE-dextran; RNA/dextran; ssDNA/heparin; RNA/heparin), lipids (ssDNA/DiO; RNA/DiO), proteins (RNA/HRP) or co-factors (ssDNA/ATP) indicated that the DEAE-dextran, DiO, ATP and heparin were preferentially enriched in the DDAB/trans-AzoAsp₂ domains, while ssDNA and RNA oligonucleotides were located primarily in the PDDA/trans-AzoAsp2 regions of the protocell networks (Supplementary Figs. S9-S11). We attributed the selective partitioning to differences in the internal structure and hydrophilicity of the two coacervate phases. While multivalent charge interactions facilitated the high solubility of nucleic acid polyanions in PDDA/trans-AzoAsp₂, the more amphiphilic environment of liquid crystalline

DDAB/trans-AzoAsp₂ was conducive to higher uptake levels of proteins, polysaccharides, lipids and ATP.

185

186

187

188

189

190

191

192

193

194

195

196

197

198

199

200

201

202

203

204

205

206

207

208

209

210

211

212

213

214

215

216

217

218

219

The self-sorting of biomacromolecules into discrete domains of the chain-like arrays was exploited as a mechanism for undertaking spatially localized enzyme and ribozyme transformations in the protocell networks (Fig. 4d). For example, selective loading of HRP into the DDAB/trans-AzoAsp₂ domains, followed by addition of Amplex red and hydrogen peroxide converted the substrate into resorufin, resulting in increasing levels of homogeneous red fluorescence specifically in the liquid crystalline coacervate droplets over a period of 500 s (Figs. 4e,f and Movie S2). The emission intensity from the DDAB/trans-AzoAsp2 domains was 32-fold higher than that measured in the adjacent PDDA/trans-AzoAsp2 droplets, indicating a high level of product retention in the HRP-containing reaction environment. In contrast, RNA enrichment and catalysis specifically within the PDDA/trans-AzoAsp2 domains was achieved by selective uptake of a minimal hammerhead ribozyme (HH-min) hybridized to a FRET-substrate²⁹. Cleavage of the FRET-substrate strand by HH-min liberated the fluorophore (6-carboxyfluorescein) from the quencher strand, resulting in an increase in green fluorescence intensity in the PDDA/trans-AzoAsp2 coacervate droplets with minimal transfer into the adjacent DDAB/trans-AzoAsp₂ domains (**Figs. 4g,h**).

As the above transformations did not involve significant changes in polarity between the reactants and products, substantial transfer of the latter between the different types of droplets was not observed. We conjectured that the fluid-like properties of the DDAB/trans-AzoAsp₂ and PDDA/trans-AzoAsp₂ coacervate droplets should facilitate the migration of encapsulated biomolecules between different domains in the protocell arrays if the guest solubility in the receiver droplets was energetically favoured. To generate non-equilibrium conditions in the protocell network, ssDNA was initially sequestered into a single population of DDAB/trans-AzoAsp₂ droplets prior to addition of a suspension of PDDA/trans-AzoAsp₂ droplets and formation of the protocell chains. Localized self/non-self adhesion within the regularly interspersed arrays then gave rise to contact-dependent transfer of the ssDNA from the PDDA/trans-AzoAsp₂ domains into adjacent DDAB/trans-AzoAsp₂ droplets (Fig. 4i). To validate this hypothesis, we pre-loaded TAMRA-ssDNA into DDAB/trans-AzoAsp₂ droplets, added PDDA/trans-AzoAsp₂ droplets to generate the protocell chains, and monitored the inter-droplet mobility of the oligonucleotide by recording the changes in fluorescence intensity in adjacent droplets (Fig. 4j and Movie S3). Typically, 95% of the TAMRA-ssDNA pre-loaded into the DDAB/trans-AzoAsp₂ domains was transferred into adjacent PDDA/trans-AzoAsp₂ droplets

within 8 min (**Fig. 4k**), confirming that molecular transfer was possible under non-equilibrium conditions.

222223

224

225

226

227

228

229

230

231

232

233

234

235

236

237

238

239

240

241

242

243

244

245

246

247

248

249

250

251

252

253

254

255

220

221

Stimuli-induced reconfiguration in protocell networks

We investigated two mechanisms for controlling the topographical reconfiguration of the chain-like arrays as a step towards triggering the transfer and redistribution of guest molecules from the protocell networks. Firstly, as the assembly of the regularly interspersed droplets was dictated by the interplay between different interfacial tensions, we sought to modulate the inter-droplet interactions through the adjustment of intermolecular forces specifically within the liquid crystalline DDAB/trans-AzoAsp2 domains. To achieve this, we minimized the hydrophobic interactions between the alkyl tails of DDAB by host-guest complexation with β -cyclodextrin (β -CD). Addition of β -CD to the protocell networks resulted in progressive disassembly of the DDAB/trans-AzoAsp2 droplets over a period of 10-30 mins (Fig. 5a, Supplementary Fig. S12). In contrast, the PDDA/trans-AzoAsp2 domains remained intact and increased in size by localized coalescence due to removal of the adjacent DDAB/trans-AzoAsp2 droplets from the network (Fig. 5a, Supplementary Fig. S13). Measurements of the droplet projected areas were determined by fluorescence microscopy and indicated that the DDAB/trans-AzoAsp₂ domains typically decreased by 50% from ca. 20 to 10 μm^2 after 1 min of adding β -CD and were less than 2 μm^2 in size after 10 min; in contrast the PDDA/trans-AzoAsp₂ droplets approximately doubled in area (Fig. 5b). Complete disassembly of the DDAB/trans-AzoAsp2 liquid crystalline phase occurred at higher β-CD/DDAB molar ratios (Supplementary Figs. S14, S15), resulting in release of guest molecules and transfer onto the surface of neighbouring PDDA/trans-AzoAsp₂ droplets (Figs. **5a,c**). Taken together, the results indicate that supramolecular complexation between β -CD and DDAB could be employed to selectively disassemble specific domains of the protocell networks, increase coalescence in the remaining PDDA/trans-AzoAsp2 domains and exchange guest molecules between the immiscible coacervate droplets.

We developed a second mechanism of protocell network reconfiguration based on the light-induced *trans*-to-*cis* isomerization of azobenzene within pre-organized chains of the DDAB/*trans*-AzoAsp₂ and PDDA/*trans*-AzoAsp₂ coacervate droplets (**Supplementary Figs. S16-S19**). We reasoned that the reduced hydrophobicity of *cis*-AzoAsp₂ would lower the interfacial tension between the DDAB- and PDDA-containing droplets, thereby inducing local fusion in the alternating sequence of immiscible droplets in the protocell chains. Density functional theory (DFT) calculations on *trans*- and *cis*-AzoAsp₂ (**Supplementary Fig. S20**), confirmed that the dipole moment of azobenzene increased from 6.64 D (*trans* state) to 44.08 D (*cis* state) after photoisomerization. Experimentally, UV-light irradiation of the

protocell networks over 10 min gave rise to extensive coalescence of the dissimilar droplets to produce heterogeneous larger droplets with co-localized guest molecules (**Fig. 5d** and **Movie S4**). For example, co-localization of Nile Red and HPTS was monitored by measuring changes in the Pearson's correlation constant (ρ ; 0 (correlated), 1 (non-correlation)). Specifically, regions along the protocell chains initially associated with the DDAB/trans-AzoAsp₂ domains showed a decrease in ρ from ca. 0.88 to 0.22 after photo-isomerism, confirming increased levels of spatial overlapping of the Nile Red and HPTS fluorophores (**Figs. 5e,f**). Subsequent irradiation with blue light for 15 min reverted the cis-AzoAsp₂ isomer back to trans-AzoAsp₂ as demonstrated by a re-established ρ value of 0.87 (**Fig. 5f**). Although demixing of the coacervate phases and re-segregation of the guest molecules occurred after exposure to blue light, structural re-assembly of ordered multi-component chains was not observed (**Fig. 5d**).

Protocell network-mediated biomolecular extraction and macroscale sorting

Having established that internal ordering and selectively biomolecular sequestration could be achieved in chain-like networks of immiscible and structurally dissimilar coacervate droplets, we investigated the possibility of exploiting differences in coacervate density to release and separate the interconnected droplets and their constituent biomolecular cargoes (Fig. 6a). To achieve this, we centrifuged suspensions of the protocell arrays at 15,000x g, to produce a stable three-phase system consisting of a DDAB-enriched upper coacervate layer (0.8 vol%), a dilute aqueous middle layer (98.8 vol%) and a PDDA-enriched lower coacervate layer (0.4 vol% in volume). Typical concentrations for DDAB and *trans*-AzoAsp₂ in the upper layer were 985 and 240 mM, respectively, while the lower layer consisted of PDDA (720 mM) and AzoAsp₂ (177 mM) (Fig. 6b). In both cases, the molar ratios were close to the stoichiometric ratio (4:1) required for near-neutral charge conditions. In contrast, the middle layer contained relatively low levels of DDAB (0.3 mM), PDDA (4.5 mM) and *trans*-AzoAsp₂ (0.8 mM), and no coacervate phase (Supplementary Fig. S21). Zeta potential measurements indicated that coacervate droplets present in the upper or lower layers were positively charged (+16 and + 33 mV, respectively) (Supplementary Fig. S22).

Given that the adhered micro-droplets could be mechanically released from the networks and then separated by differences in density, we used the above procedure as a protocell-based micro-extraction system for selective cargo sequestration and macroscopic sorting. As an initial test, we prepared protocell networks with alternating sequences of DDAB/trans-AzoAsp₂ and PDDA/trans-AzoAsp₂ coacervate droplets loaded with FITC-HRP or TAMRA-ssDNA, respectively, and centrifuged the suspensions. Compositional analysis of the separated layers indicated that the guest molecules were retained by their respective

coacervate phases after centrifugation, with negligible amounts detected in the aqueous middle layer. Typically, the concentration of FITC-HRP in the DDAB-containing upper layer was approximately 8-fold higher than in the PDDA-containing lower layer, while the TAMR-ssDNA concentration in the lower layer was approximately 12-fold higher than that in the upper layer (Fig. 6c). Fluorescence microscopy images of individual coacervate micro-droplets extracted from the upper or lower layers confirmed the selective partitioning of the guest biomolecules (Figs. 6d,e). Based on the above results, we used the protocell networks for the biomolecular extraction and macroscale sorting from mixtures of oligonucleotides with polysaccharides (DEAE-dextran/ssDNA), lipids (DiO/ssDNA) or co-factors (ATP/ssDNA), as well as using different dye molecules (Nile Red or HPTS) (Supplementary Fig. S23). DEAE-dextran, DiO, ATP and Nile Red were partitioned into the DDAB/trans-AzoAsp₂ coacervate upper layer at approximately 50-, 25-, 20- or 13-fold higher concentrations than in the PDDA/trans-AzoAsp2 lower layer (Supplementary Fig. S24). In contrast, ssDNA and HPTS concentrations in the PDDA-enriched coacervate lower layer after centrifugation were approximately 7-, 20-, 13- or 20-fold higher than observed in the upper layer.

308309

310

311

312

313

314

315

316

317

318

319

320

321

322

323

324

325

326

327

292

293

294

295

296

297

298

299

300

301

302

303

304

305

306

307

Conclusions

In summary, we describe a new type of protocell network based on an interactive binary population of immiscible coacervate micro-droplets. The membrane-less coacervate droplets are produced by associative liquid-liquid phase separation and have either liquid-crystalline (DDAB/trans-AzoAsp₂) or homogeneous (PDDA/trans-AzoAsp₂) interiors with increased levels of hydrophobicity or hydrophilicity, respectively. Interactions between coacervate droplets with similar structures lead to fusion while contact between structurally disparate droplets results in adhesion. Consequently, heterogeneous aggregates of the dissimilar droplets spontaneously rearrange and develop over 60 min into chain-like superstructures with an alternating sequence of liquid crystalline and non-structured coacervate droplet micro-domains with hemi-spherical junctions. This process is facilitated by the reduced dimensionality associated with slow sedimentation of the coacervate droplets and primary aggregates onto pegylated glass coverslips. By recruiting different biomacromolecules into specific domains of the protocell chains we exploit the superstructures as a model protocell network capable of macromolecular self-sorting, spatially localized enzyme/ribozyme biocatalysis and inter-droplet molecular translocation. We also show that the networks can be topologically reconfigured by using host-guest complexation to selectively disassemble the DDAB/trans-AzoAsp₂ domains. Alternatively, photo-isomerisation of AzoAsp₂ by exposure to UV or blue light fuses the immiscible coacervate droplets along the chains and controls the spatial distribution of guest molecules. Finally, as proof-of-concept we develop a protocell network-based micro-extraction and macroscale biomolecular sorting system.

Taken together, the self-assembly of multi-component coacervate-based protocell networks provides a step towards the spontaneous construction of cytomimetic systems with higher-order organization and collective functionality. The networks are thermodynamic constructs, being driven by the surface energy minimization of the DDAB/trans-AzoAsp₂ and PDDA/trans-AzoAsp₂ droplets in a restraining force field generated by the local surface adhesion interactions. Currently, the superstructures are structurally stable for at least 30 days at room temperature, and it should be possible to increase their lifetime for example by post-assembly membranization of the coacervate droplets¹⁸⁻²¹. Moreover, increasing the length of the chains and reducing their polydispersity should be possible by implementing greater control over the nucleation and growth kinetics of coacervate droplet adhesion and fusion. In the longer-term, manipulating the chains into interconnected macroscale structures using micro-fabricated surfaces or flow chambers could provide an unprecedented approach to the design and construction of artificial multicellular colonies and tissues with embedded circuitry and information processing.

345 346

347

348

328

329

330

331

332

333

334

335

336

337

338

339

340

341

342

343

344

Acknowledgements

This work was supported by the National Natural Science Foundation of China (22072159 and 22172007), the Fundamental Research Funds for the Central Universities (buctrc202015) 349 for financial support. S.M. was funded by the ERC Advanced Grant Scheme (EC-2016-674 ADG 740235).

350 351 352

Conflict of Interest

353 The authors declare no competing interest.

354 355

356

357

358

Author Contributions

W.J. and L.J. performed the experiments, analysed the data and wrote the manuscript. M.Z. and J. W. performed computational experiments. Y.L., S.M. and Y.Q. conceived, designed and supervised the study, analysed the data and wrote the manuscript. All authors discussed the results and commented on the manuscript.

359 360

363

364

361 362

References

Buddingh, B. C., Elzinga, J. & van Hest, J. C. M. Intercellular communication between artificial cells by allosteric amplification of a molecular signal. Nat. Commun. 11, 1652 (2020).

- Booth, M. J., Schild, V. R., Graham, A. D., Olof, S. N. & Bayley, H. Light-activated communication in synthetic tissues. *Sci. Adv.* **2**, e1600056 (2016).
- 367 3 Tian, L., Li, M., Patil, A. J., Drinkwater, B. W. & Mann, S. Artificial morphogen-mediated differentiation in synthetic protocells. *Nat. Commun.* **10**, 3321 (2019).
- Gao, N. et al. Chemical-mediated translocation in protocell-based microactuators. *Nat. Chem.* **13**, 868–879 (2021).
- 371 5 Adamala, K. P., Engelhart, A. E. & Szostak, J. W. Collaboration between primitive cell membranes and soluble catalysts. *Nat. Commun.* **7**, 11041 (2016).
- 373 6 Bhattacharya, A., Cho, C. J., Brea, R. J. & Devaraj, N. K. Expression of fatty acyl-CoA ligase drives one-pot de novo synthesis of membrane-bound vesicles in a cell-free transcription-translation system. *J. Am. Chem. Soc.* **143**, 11235–11242 (2021).
- 376 Saha, R., Verbanic, S. & Chen, I. A. Lipid vesicles chaperone an encapsulated RNA aptamer.
 377 *Nat. Commun.* **9**, 2313 (2018).
- Marguet, M., Bonduelle, C. & Lecommandoux, S. Multicompartmentalized polymeric systems: towards biomimetic cellular structure and function. *Chem. Soc. Rev.* **42**, 512–529 (2013).
- Peters, R. J., Louzao, I. & van Hest, J. C. M. From polymeric nanoreactors to artificial organelles. *Chem. Sci.* **3**, 335–342 (2012).
- Huang, X. et al. Interfacial assembly of protein-polymer nano-conjugates into stimulus-responsive biomimetic protocells. *Nat. Commun.* **4**, 2239 (2013).
- Li, M., Harbron, R. L., Weaver, J. V., Binks, B. P. & Mann, S. Electrostatically gated membrane permeability in inorganic protocells. *Nat. Chem.* **5**, 529–536 (2013).
- Torre, P., Keating, C. D. & Mansy, S. S. Multiphase water-in-oil emulsion droplets for cell-free transcription-translation. *Langmuir* **30**, 5695–5699 (2014).
- Wu, H., Du, X., Meng, X., Qiu, D. & Qiao, Y. A three-tiered colloidosomal microreactor for continuous flow catalysis. *Nat. Commun.* **12**, 6113 (2021).
- Mukwaya, V. et al. Lectin-glycan-mediated nanoparticle docking as a step toward programmable membrane catalysis and adhesion in synthetic protocells. *ACS Nano.* **14**, 7899–7910 (2020).
- Mukwaya, V. et al. Programmable membrane-mediated attachment of synthetic virus-like nanoparticles on artificial protocells for enhanced immunogenicity. *Cell Rep. Phys. Sci.* **2**, 100291 (2021).
- Koga, S., Williams, D. S., Perriman, A. W. & Mann, S. Peptide-nucleotide microdroplets as a step towards a membrane-free protocell model. *Nat. Chem.* **3**, 720–724 (2011).
- 398 Yewdall, N. A., André, A. A., Lu, T. & Spruijt, E. Coacervates as models of membraneless organelles. *Curr. Opin. Colloid Interface Sci.* **52**, 101416 (2021).
- 400 18 Liu, S. et al. Enzyme-mediated nitric oxide production in vasoactive erythrocyte 401 membrane-enclosed coacervate protocells. *Nat. Chem.* **12**, 1165–1173 (2020).
- 402 19 Pir Cakmak, F., Marianelli, A. M. & Keating, C. D. Phospholipid membrane formation templated by coacervate droplets. *Langmuir* **37**, 10366–10375 (2021).
- 404 20 Gao, N., Xu, C., Yin, Z., Li, M. & Mann, S. Triggerable protocell capture in nanoparticle-caged coacervate microdroplets. *J. Am. Chem. Soc.* **144**, 3855–3862 (2022).
- Zhang, Y. et al. Giant coacervate vesicles as an integrated approach to cytomimetic modeling. J. Am. Chem. Soc. **143**, 2866–2874 (2021).
- Weitz, M. et al. Diversity in the dynamical behaviour of a compartmentalized programmable biochemical oscillator. *Nat. Chem.* **6**, 295–302 (2014).
- Sokolova, E. et al. Enhanced transcription rates in membrane-free protocells formed by coacervation of cell lysate. *Proc. Natl. Acad. Sci. U. S. A.* **110**, 11692–11697 (2013).
- Dubuc, E. et al. Cell-free microcompartmentalised transcription-translation for the prototyping of synthetic communication networks. *Curr. Opin. Biotechnol.* **58**, 72–80 (2019).

- 25 Zhu, T. F. & Szostak, J. W. Coupled growth and division of model protocell membranes. *J. Am. Chem. Soc.* **131**, 5705–5713 (2009).
- Nakashima, K. K., van Haren, M. H., André, A. A., Robu, I. & Spruijt, E. Active coacervate droplets are protocells that grow and resist Ostwald ripening. *Nat. Commun.* **12**, 3819 (2021).
- 418 27 Kurihara, K. *et al.* Self-reproduction of supramolecular giant vesicles combined with the amplification of encapsulated DNA. *Nat. Chem.* **3**, 775–781 (2011).
- 420 28 Elani, Y., Law, R. V. & Ces, O. Vesicle-based artificial cells as chemical microreactors with 421 spatially segregated reaction pathways. *Nat. Commun.* **5**, 5305 (2014).
- Drobot, B. et al. Compartmentalised RNA catalysis in membrane-free coacervate protocells.

 Nat. Commun. 9, 3643 (2018).
- 424 30 Iglesias-Artola, J. M. et al. Charge-density reduction promotes ribozyme activity in RNA-peptide coacervates via RNA fluidization and magnesium partitioning. *Nat. Chem.* **14**, 407–416 (2022).
- Donau, C. et al. Active coacervate droplets as a model for membraneless organelles and protocells. *Nat. Commun.* **11**, 5167 (2020).
- Wilson, D. A., Nolte, R. J. & Van Hest, J. C. M. Autonomous movement of platinum-loaded stomatocytes. *Nat. Chem.* **4**, 268–274 (2012).
- 431 33 Kumar, B., Patil, A. J. & Mann, S. Enzyme-powered motility in buoyant organoclay/DNA protocells. *Nat. Chem.* **10**, 1154–1163 (2018).
- Rodríguez-Arco, L., Li, M. & Mann, S. Phagocytosis-inspired behaviour in synthetic protocell communities of compartmentalized colloidal objects. *Nat. Mater.* **16**, 857–863 (2017).
- 435 35 Qiao, Y., Li, M., Booth, R. & Mann, S. Predatory behaviour in synthetic protocell communities. 436 Nat. Chem. **9**, 110–119 (2017).
- 437 36 Qiao, Y., Li, M., Qiu, D. & Mann, S. Response-retaliation behavior in synthetic protocell communities. *Angew. Chem. Int. Ed.* **131**, 17922–17927 (2019).
- 439 37 Merindol, R., Loescher, S., Samanta, A. & Walther, A. Pathway-controlled formation of 440 mesostructured all-DNA colloids and superstructures. *Nat. Nanotechnol.* **13**, 730–738 (2018).
- 441 38 Villar, G., Graham, A. D. & Bayley, H. A tissue-like printed material. *Science* **340**, 48–52 (2013).
- 442 39 Alcinesio, A. et al. Controlled packing and single-droplet resolution of 3D-printed functional synthetic tissues. *Nat. Commun.* **11**, 2105 (2020).
- 444 40 Booth, M. J., Restrepo Schild, V., Box, S. J. & Bayley, H. Light-patterning of synthetic tissues 445 with single droplet resolution. *Sci. Rep.* **7**, 9315 (2017).
- Tian, L. et al. Spontaneous assembly of chemically encoded two-dimensional coacervate droplet arrays by acoustic wave patterning. *Nat. Commun.* **7**, 13068 (2016).
- 448 42 Yang, Z., Wei, J., Sobolev, Y. I. & Grzybowski, B. A. Systems of mechanized and reactive droplets powered by multi-responsive surfactants. *Nature* **553**, 313–318 (2018).
- 450 43 Dupin, A. & Simmel, F. C. Signalling and differentiation in emulsion-based 451 multi-compartmentalized in vitro gene circuits. *Nat. Chem.* **11**, 32–39 (2019).
- 452 44 Ramsay, K., Levy, J., Gobbo, P. & Elvira, K. S. Programmed assembly of bespoke prototissues on a microfluidic platform. *Lab. Chip.* **21**, 4574–4585 (2021).
- Deshpande, S. et al. Spatiotemporal control of coacervate formation within liposomes. *Nat. Commun.* **10**, 1800 (2019).
- 456 46 Gobbo, P. et al. Programmed assembly of synthetic protocells into thermoresponsive 457 prototissues. *Nat. Mater.* **17**, 1145–1153 (2018).
- Galanti, A. et al. A floating mold technique for the programmed assembly of protocells into protocellular materials capable of non-equilibrium biochemical sensing. *Adv. Mater.* **33**, 2100340 (2021).
- 461 48 Liu, J. et al. Hydrogel-immobilized coacervate droplets as modular microreactor assemblies. 462 Angew. Chem. Int. Ed. **59**, 6853–6859 (2020).

- 463 49 Funasaki, N. & Neya, S. Multiple complexation of didecyldimethylammonium bromide and cyclodextrins deduced from electromotive force measurements. *Langmuir* **16**, 5343–5346 465 (2000).
- Mu, W. et al. Membrane-confined liquid-liquid phase separation toward artificial organelles. Sci. Adv. 7, eabf9000 (2021).
- Fraccia, T. P. & Jia, T. Z. Liquid crystal coacervates composed of short double-stranded DNA and cationic peptides. *ACS Nano.* **14**, 15071–15082 (2020).
- Jing, H. et al. Fission and internal fusion of protocell with membraneless "organelles" formed by liquid-liquid phase separation. *Langmuir* **36**, 8017–8026 (2020).
- 53. Fisher, R. S., Elbaum-Garfinkle, S. Tunable multiphase dynamics of arginine and lysine liquid condensates. *Nat. Commun.* **11**, 4628 (2020).
- 474 54 Lu, T. & Spruijt, E. Multiphase complex coacervate droplets. *J. Am. Chem. Soc.* **142**, 2905–2914 475 (2020).
- Kaur, T. et al. Sequence-encoded and composition-dependent protein-RNA interactions control multiphasic condensate morphologies. *Nat. Commun.* **12**, 872 (2021).

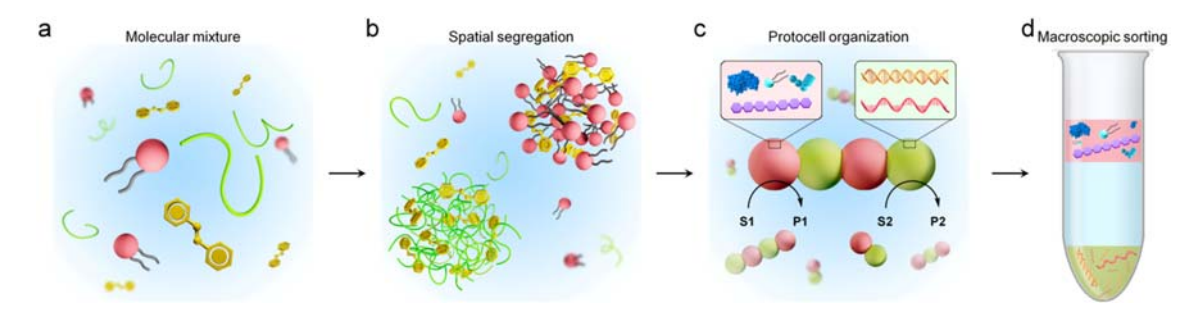
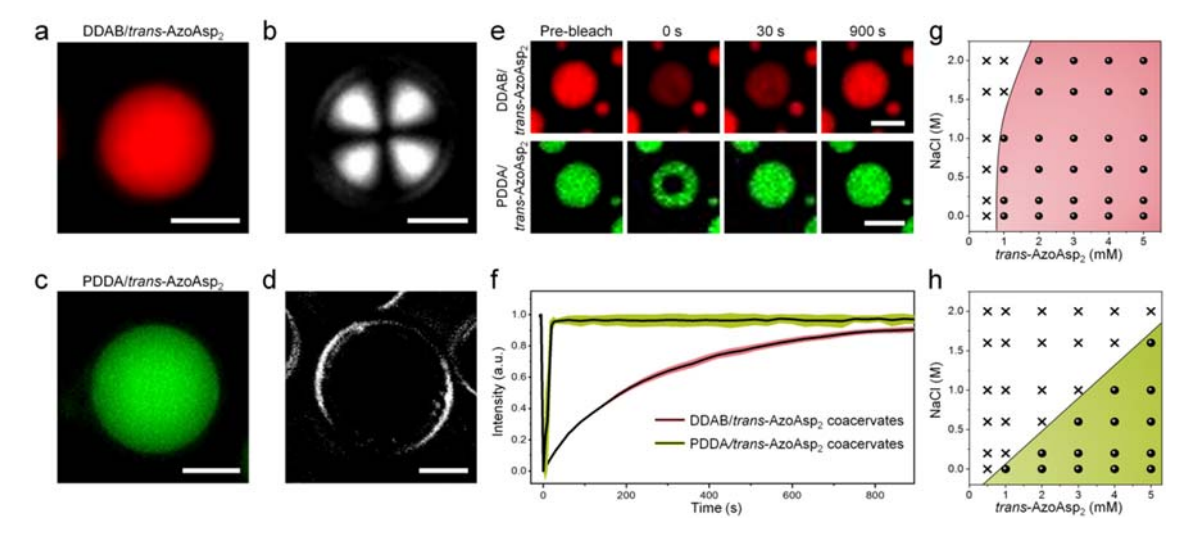


Figure 1. Spontaneous assembly, spatial segregation, self-organization, and macroscopic sorting of coacervate-based protocell networks. (a,b) Mixing of DDAB (red), PDDA (green) and *trans*-AzoAsp₂ (brown) (a), results in associative LLPS and spontaneous spatial segregation to give a binary population of immiscible DDAB/*trans*-AzoAsp₂ and PDDA/*trans*-AzoAsp₂ coacervate micro-droplets (b). (c) Localized self/non-self adhesion and self/self fusion within mixed droplet aggregates produces self-organized chain-like networks with an alternating sequence of interconnected droplets and contiguous hemi-spherical contacts. Biomolecules are selectively partitioned within the DDAB/*trans*-AzoAsp₂ (red) and PDDA/*trans*-AzoAsp₂ (green) coacervate droplets to generate integrated higher-order protocell assemblies capable of macromolecular self-sorting, spatially localized biocatalysis (substrate S1/product P1 and S2/P2) and inter-droplet molecular transfer. The networks are recnfigured by chemical or photochemical stimuli. (d) Centrifugation of the protocell networks results in biomolecular extraction and macroscopic sorting via a three-layer separation process; DDAB/*trans*-AzoAsp₂ (upper layer), depleted aqueous phase (middle layer) and PDDA/*trans*-AzoAsp₂ (lower layer).



501

502

503

504

505

506

507

508

509

510

511

512

513

514

515

Figure 2. Protocell network components. (a,b) Fluorescence microscopy (a) and optical polarized microscopy (b) images of DDAB/trans-AzoAsp₂ coacervate droplets (molar ratio = 4 : 1; Nile Red hydrophobic stain, red fluorescence). A birefringent Maltese cross pattern is shown in (b), indicating liquid crystalline order. (c,d) Fluorescence microscopy (c) and polarized microscopy (d) images of PDDA/trans-AzoAsp₂ coacervate droplets (molar ratio = 4 : 1; hydrophilic HPTS, green fluorescence). No internal order is observed. (e,f) FRAP monitoring of Nile Red-loaded DDAB/trans-AzoAsp2 (top) and HPTS-loaded PDDA/trans-AzoAsp2 (bottom) coacervate droplets. Time-dependent fluorescence microscopy images (e), and corresponding kinetics of fluorescence recovery (f) of Nile Red-loaded DDAB/trans-AzoAsp2 (top) and HPTS-loaded PDDA/trans-AzoAsp2 (bottom) coacervate droplets; the data are consistent with liquid crystalline and homogeneous coacervate structures, respectively. Error bars; SDs of three replicas. Scale bars; a-d, e, 5 μm. (g,h) Phase diagrams for DDAB/trans-AzoAsp2 (e) and PDDA/trans-AzoAsp2 (f) mixtures prepared in the absence/presence of NaCl. Shaded regions denote conditions under which coacervate micro-droplets were observable. Liquid crystalline DDAB/trans-AzoAsp2 droplets remain intact in the presence of 2 M sodium chloride while the more hydrophilic PDDA/trans-AzoAsp₂ droplets disassemble under the same conditions. Concentrations; DDAB (4 mM), PDDA (4 mM), AzoAsp₂ (0.5-5 mM) and NaCl (0-2 M).

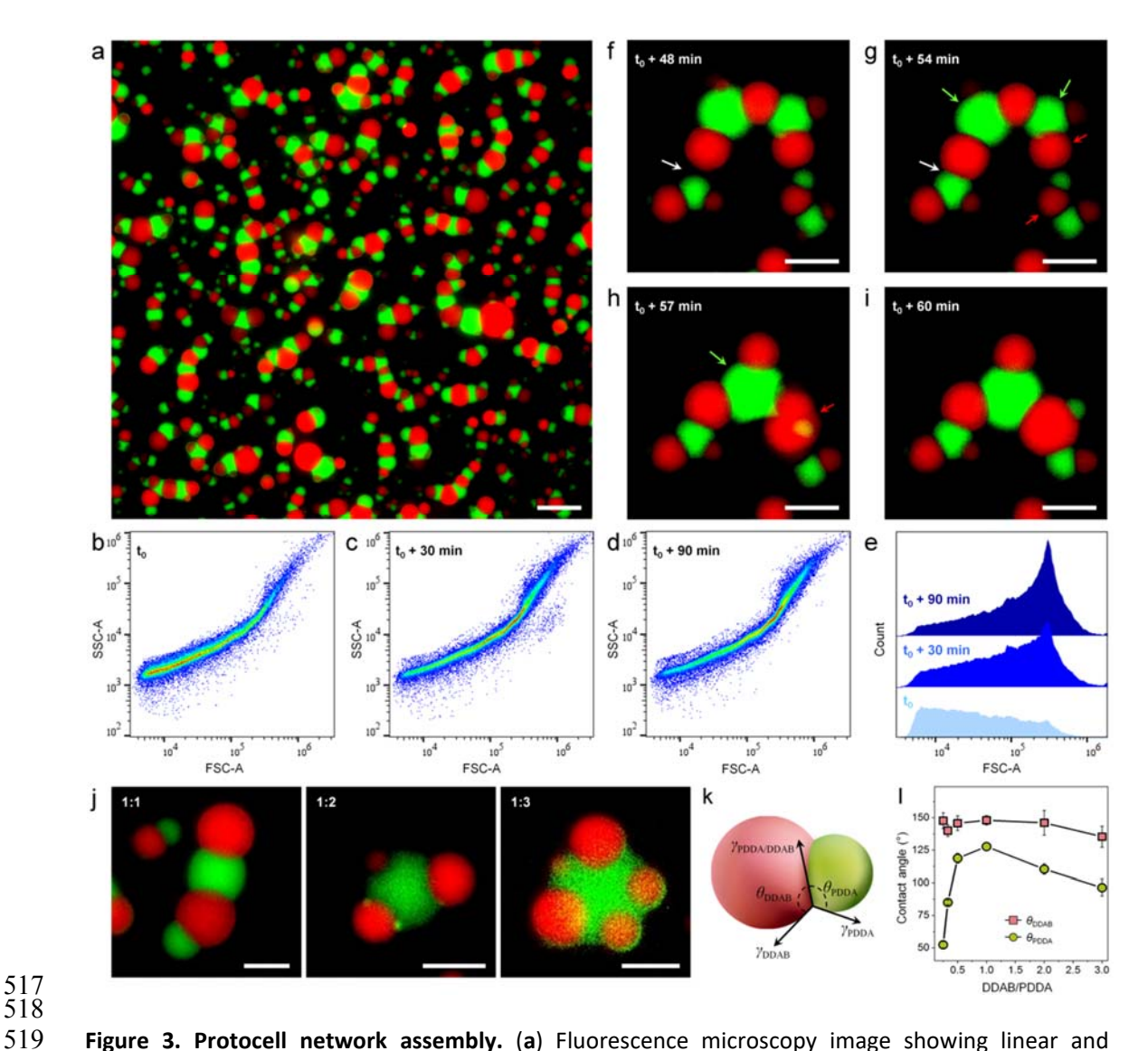


Figure 3. Protocell network assembly. (a) Fluorescence microscopy image showing linear and branched chain-like assemblies of alternating Nile Red-loaded DDAB/trans-AzoAsp2 (red fluorescence) and HPTS-loaded PDDA/trans-AzoAsp₂ (green fluorescence) interconnected coacervate micro-droplets (DDAB: PDDA: trans-AzoAsp2 molar ratio = 4:4:2. (b-d) FACS time series of FSC-A versus SSC-A dot plots for coexisting DDAB/trans-AzoAsp2 and PDDA/trans-AzoAsp2 coacervate droplets after mixing in the dark (t_0) (b), $t_0 + 30$ min (c) and $t_0 + 90$ min (d). Formation of the chain-like assemblies after 30 min gives rise to a specific increase in scattering (red domain) in a localized region of the pseudo-color plots; (n = 100,000). (e) Corresponding plots of counts against FSC-A values at different times. (f-i) Time-series of fluorescence microscopy images showing spontaneous self/non-self droplet adhesion (white arrows in f and g) and self/self droplet fusion (red and green arrows in g and h) to produce a stabilized chain with alternating DDAB/trans-AzoAsp2 (red) and PDDA/trans-AzoAsp₂ (green) coacervate droplets (i). (j) Protocell network assembly at DDAB: PDDA molar ratios of 1:1, 1:2 and 1:3 showing large more diffuse PDDA/trans-AzoAsp₂ droplets (green) at higher PDDA concentrations. Staining as in a. (k,l) Graphics showing contact points associated with interfacial tensions (γ_{DDAB} , γ_{PDDA} and $\gamma_{DDAB/PDDA}$) and contact angles (θ_{DDAB} and θ_{PDDA}) (k), and plots of (θ_{DDAB} and θ_{PDDA}) against DDAB/PDDA molar ratio (I). Scale bars: $\mathbf{a} = 10 \, \mu \text{m}$; $\mathbf{f} = 5 \, \mu \text{m}$; $\mathbf{j} = 10 \, \mu \text{m}$; $\mathbf{f} = 10 \, \mu \text{m}$; 5 μm.

521

522

523

524

525

526

527

528

529

530

531

532

533

534

535

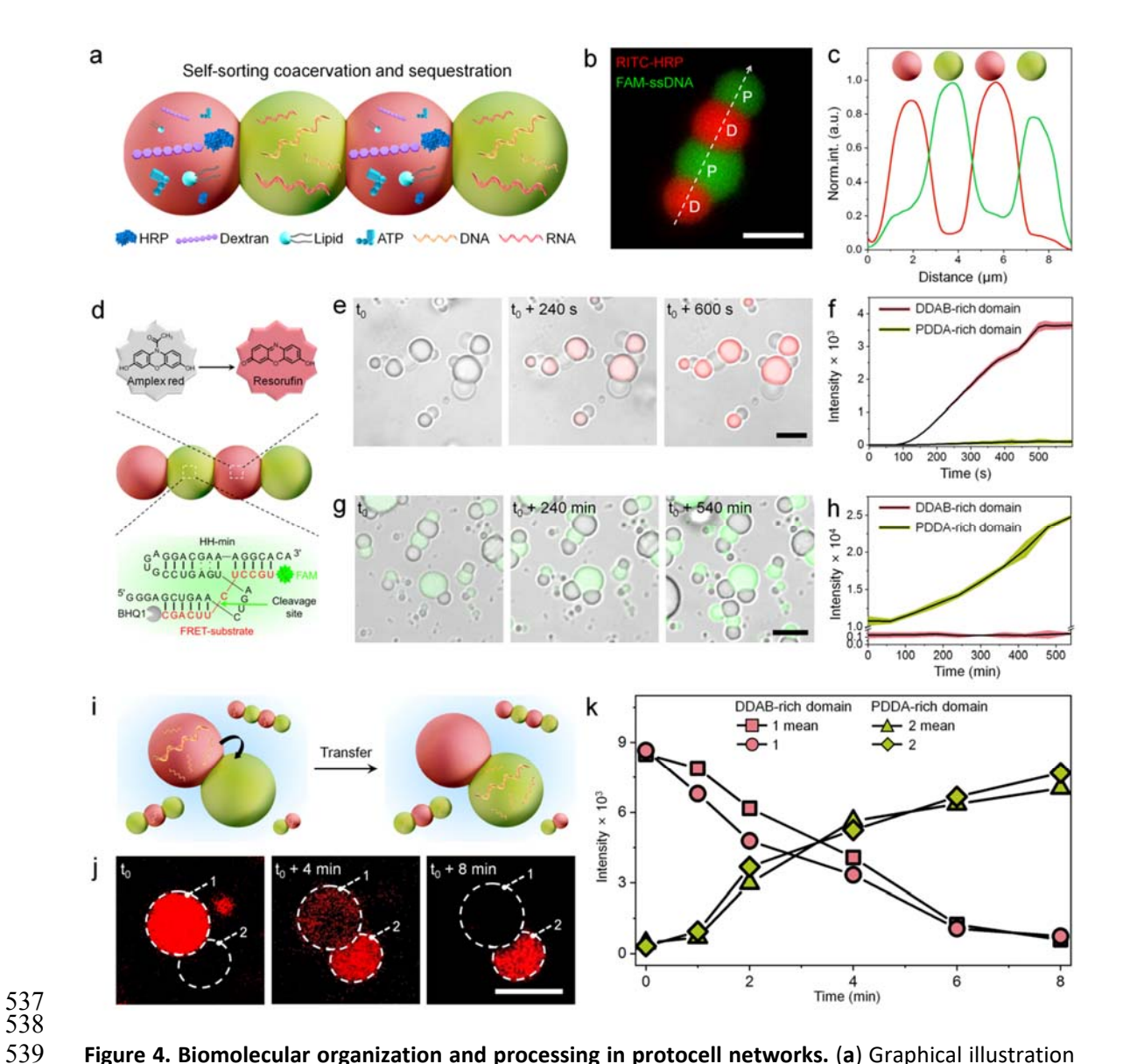


Figure 4. Biomolecular organization and processing in protocell networks. (a) Graphical illustration showing higher-order multi-component protocell model. Spontaneous self-sorting of enzymes (HRP), polysaccharides (dextran), lipids (DiO), co-factors (ATP), and single-stranded polynuclotides (DNA and RNA) in linked chains of alternating DDAB/trans-AzoAsp2 (red) and PDDA/trans-AzoAsp2 (green) coacervate micro-droplets occurs by spatially selective molecular partitioning, leading to regiospecific properties and chemical processing. (b) Fluorescence microscopy image of a single chain of regularly interspersed DDAB/trans-AzoAsp2 (D) and PDDA/trans-AzoAsp2 (P) coacervate micro-droplets showing selective partitioning of RITC-HRP (red fluorescence) or FAM-ssDNA (green fluorescence) in the **D** and **P** domains, respectively, of the interconnected network. (c) Corresponding fluorescence intensity line profile (dashed line in b) showing alternating sequence of RITC-HRP (red line) and FAM-ssDNA (green line) enriched specifically in the D and P droplets. (d) Schematic showing spatially organized biomolecular processing in protocell networks. Enzyme (HRP) or ribozyme (HH-min) transformations occur in an alternating sequence of interconnected DDAB/trans-AzoAsp₂ (red) and PDDA/trans-AzoAsp₂ (green) coacervate micro-droplets. HRP-mediated peroxidation of Amplex Red to resorufin (red fluorescence) takes place specifically in the DDAB/trans-AzoAsp₂ droplets, while HH-mediated cleavage of a FRET-ssRNA substrate to release

541

542

543

544

545

546

547

548

549

550

551

552

553

a green fluorescence probe is localized within the PDDA/trans-AzoAsp2 droplets. (e,f) Time-lapse fluorescence microscopy images (e) and corresponding red fluorescence intensity changes with time (f) for HRP/H₂O₂-mediated peroxidation in coacervate-based protocell networks. Resorufin (red fluorescence) is produced and retained specifically within the DDAB/trans-AzoAsp2 domains. (g,h) Time-lapse fluorescence microscopy images (g) and corresponding green fluorescence intensity changes with time (h) for HH-min cleavage and release and retention of the FRET-substrate (green fluorescence) specifically within the PDDA/trans-AzoAsp₂ domains. (i) Schematic showing inter-droplet transfer of ssDNA within a chain of alternating coacervate-based protocells; migration occurs from the DDAB/trans-AzoAsp2 to PDDA/trans-AzoAsp2 domains due to increased solubility of the oligonucleotide in the PDDA-containing matrix. ssDNA is initially sequestered into a single population of DDAB/trans-AzoAsp₂ droplets prior to addition of a suspension of PDDA/trans-AzoAsp₂ droplets and self-assembly of the regularly interspersed droplet arrays. (j,k) Time-lapse fluorescence microscopy images (j) and corresponding red fluorescence intensity changes with time (k) showing transfer of TAMRA-ssDNA from a DDAB/trans-AzoAsp₂ droplet (1) to an adjacent PDDA/trans-AzoAsp2 domain (2) located in the same protocell chain; fluorescence intensity values at positions 1 and 2, and mean fluorescence values for droplets 1 and 2 are plotted. Scale bars: b = 3 μm ; **e**, **g**, **j** = 5 μm .

555

556

557

558

559

560

561

562

563

564

565

566

567

568

569

570

571

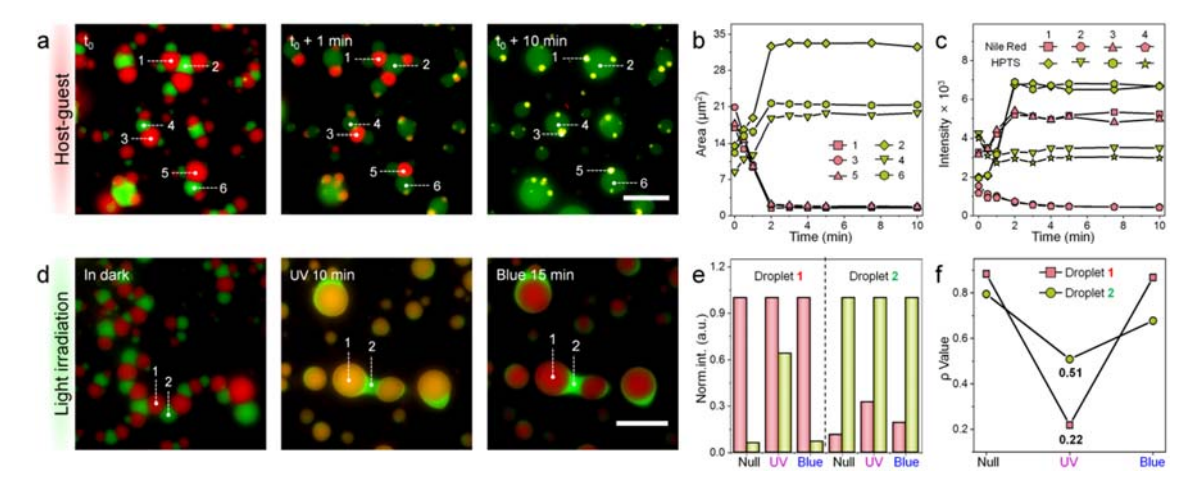


Figure 5. Stimuli-induced reconfiguration in protocell networks. (a-c) Reconfiguration of protocell networks by β-CD-mediated disassembly of DDAB/trans-AzoAsp2 domains showing progressive disassociation of Nile Red-loaded DDAB/trans-AzoAsp2 domains (red) accompanied by local fusion of HPTS-loaded PDDA/trans-AzoAsp2 droplets (green) (a); corresponding time-dependent plots of domain sizes and fluorescence intensities for various marked droplets (b,c). High localized concentrations of HPTS (green) and Nile Red (yellow) are observed in the DDAB/trans-AzoAsp2 droplets 10 min after addition of β-CD ([β-CD]/[DDAB] = 6). (d-f) Reconfiguration of protocell networks by light-mediated trans-to-cis isomerization of azobenzene in internally ordered networks of Nile Red-loaded DDAB/trans-AzoAsp2 (red) and HPTS-loaded PDDA/trans-AzoAsp2 droplets (green). Fluorescence images recorded after samples were left in the dark (left), 10 min after UV irradiation (middle), or 10 min UV followed by 15 min in blue light (right) (d). Corresponding measurements of normalized red and green fluorescence intensities (e) and changes in Pearson's correlation coefficient (ρ) (f) are also shown. UV-induced destabilization results in inter-droplet fusion and guest molecular mixing, while blue light restores the segregation of Nile Red and HPTS. Scale bars: 10 μm.

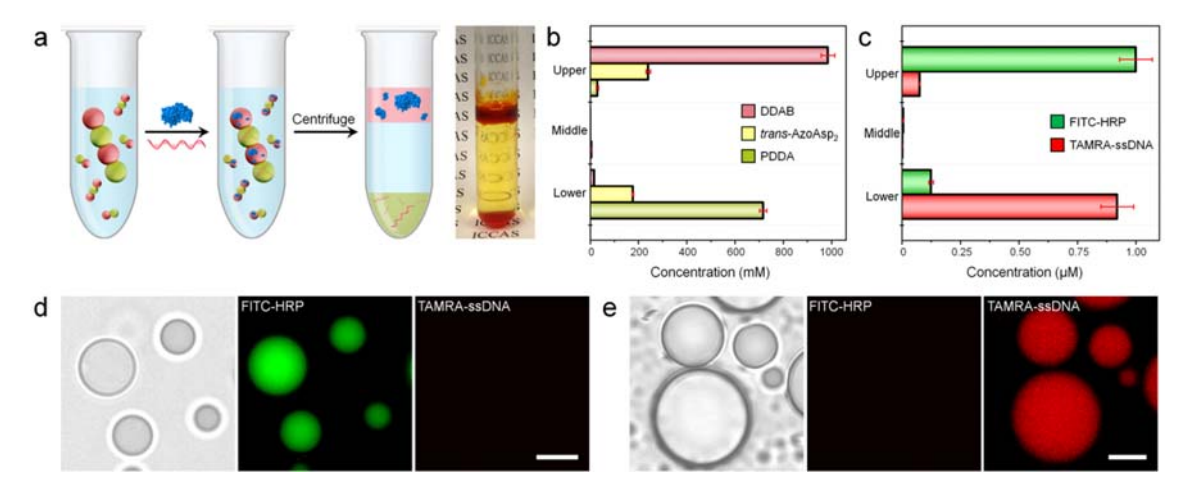


Figure 6. Protocell network-mediated biomolecular extraction and macroscale sorting. (a) Selective uptake and spatial segregation of various guest biomolecules in protocell networks comprising an alternating sequence of coacervate droplet domains followed by centrifugation results in a lower density upper layer of DDAB/trans-AzoAsp2-enriched coacervate droplets, a dilute aqueous middle layer and a higher density PDDA/trans-AzoAsp2-enriched coacervate droplet lower layer. The partitioned biomolecular cargos are sorted between the upper and lower layers (photograph, far right) according to their selective partitioning in the immiscible coacervate droplets. (b,c) Compositional analysis of coacervate host components by 1 H NMR spectroscopy (b) and analysis of guest components (FITC-HRP or TAMRA-ssDNA) by fluorescence spectroscopy (c) in the three separated layers; the molar ratio of DDAB/trans-AzoAsp2 and PDDA/trans-AzoAsp2 in the upper and lower layers is close to 4:1 (charge neutralization) and FITC-HRP and TAMRA-ssDNA are efficiently sorted into the DDAB- or PDDA-enriched layers, respectively. (d-e) Optical and fluorescence microscopy images of coacervate droplets obtained from the upper (d) or lower (e) layers after centrifugation showing extraction and sorting of FITC-HRP and TAMRA-ssDNA, respectively. Scale bars, 5 μ m.